

Stable perovskite single-crystal X-ray imaging detectors with single-photon sensitivity

Received: 13 December 2022

Accepted: 30 March 2023

Published online: 8 May 2023

Check for updates

Kostiantyn Sakhatskyi ^{1,2,6}, Bekir Turedi ^{1,2,3,6}, Gebhard J. Matt ^{1,2}, Erfu Wu ⁴, Anastasiia Sakhatska ^{1,2}, Vitalii Bartosh ^{1,2}, Muhammad Naufal Lintangpradipto³, Rounak Naphade ³, Ivan Shorubalko ⁴, Omar F. Mohammed ^{3,5}, Sergii Yakunin ^{1,2} , Osman M. Bakr ³ & Maksym V. Kovalenko ^{1,2}

A major thrust of medical X-ray imaging is to minimize the X-ray dose acquired by the patient, down to single-photon sensitivity. Such characteristics have been demonstrated with only a few direct-detection semiconductor materials such as CdTe and Si; nonetheless, their industrial deployment in medical diagnostics is still impeded by elaborate and costly fabrication processes. Hybrid lead halide perovskites can be a viable alternative owing to their facile solution growth. However, hybrid perovskites are unstable under high-field biasing in X-ray detectors, owing to structural lability and mixed electronic–ionic conductivity. Here we show that both single-photon-counting and long-term stable performance of perovskite X-ray detectors are attained in the photovoltaic mode of operation at zero-voltage bias, employing thick and uniform methylammonium lead iodide single-crystal films (up to 300 μm) and solution directly grown on hole-transporting electrodes. The operational device stability exceeded one year. Detection efficiency of 88% and noise-equivalent dose of 90 pGy_{air} are obtained with 18 keV X-rays, allowing single-photon-sensitive, low-dose and energy-resolved X-ray imaging. Array detectors demonstrate high spatial resolution up to 11 lp mm^{-1} . These findings pave the path for the implementation of hybrid perovskites in low-cost, low-dose commercial detector arrays for X-ray imaging.

For a semiconductor to serve as a direct X-ray detector capable of single-photon counting, several requirements must be fulfilled: high resistivity ($\leq 10^{10}$ $|\Omega| \text{ cm}$) and hence sufficiently low noise levels for resolving charges generated by a single photon, a high carrier mobility–lifetime ($\mu\tau$) product for the efficient collection of photon-generated

carriers and the absorption of (nearly) all X-ray photons—the latter scales with the thickness and average atomic number (Z) of the constituent elements. Very few high- Z semiconductors were proposed to fulfil these requirements at room temperature^{1–7} and thus far, only costly, ultrapure CdTe and CdZnTe single crystals, usually grown from

¹Laboratory of Inorganic Chemistry, Department of Chemistry and Applied Biosciences, ETH Zürich, Zürich, Switzerland. ²Laboratory for Thin Films and Photovoltaics, Empa—Swiss Federal Laboratories for Materials Science and Technology, Dübendorf, Switzerland. ³KAUST Catalysis Center (KCC), Division of Physical Sciences and Engineering, King Abdullah University of Science and Technology (KAUST), Thuwal, Kingdom of Saudi Arabia.

⁴Laboratory for Transport at Nanoscale Interfaces, Empa—Swiss Federal Laboratories for Materials Science and Technology, Dübendorf, Switzerland.

⁵Advanced Membranes and Porous Materials Center, Division of Physical Science and Engineering, King Abdullah University of Science and Technology, Thuwal, Kingdom of Saudi Arabia. ⁶These authors contributed equally: Kostiantyn Sakhatskyi, Bekir Turedi. e-mail: yakunins@ethz.ch; osman.bakr@kaust.edu.sa; mvkovalenko@ethz.ch

a melt by high-pressure Bridgman or Czochralski methods, have been commercially deployed^{8,9}. Lead halide perovskite semiconductors (general formula of APbX₃, where A is a cation, either organic methylammonium (MA⁺) or formamidinium, or inorganic Cs⁺; and X is an anion of I, Br or Cl halogen) are the most intensely studied class of contender high-Z materials for high-energy photon detection^{4,10–24}. Excellent electronic characteristics are commonplace with both inexpensive solution growth techniques (for all A cations)^{4,17,24} and melt growth techniques (CsPbBr₃ or CsPbCl₃)^{21,25}, often using the conventional purity of precursors. Calculated X-ray absorption coefficients are even a few-fold higher compared with CdTe for soft X-rays (Extended Data Fig. 1).

We find that the major question, pertaining to the eventual utility of perovskites as commercial X-ray detectors, is the demonstration of simultaneously stable operation and near-ideal detection efficiency (DE) of such devices. Even for high-Z and high- $\mu\tau$ materials such as CdTe and APbI₃ perovskites, the required collection of photocarriers requires high voltages of hundreds to thousands of volts applied across material thicknesses ranging from millimetres to centimetres (depending on the detected photon energies, which range from tens to hundreds of kiloelectronvolts). The long-term operational stability is mainly limited by the stability of the semiconductor and interfaces under such high electric bias. The issue is especially acute for perovskites, as they are mixed electronic–ionic conductors, in which high dark currents and unstable performance often arise from the ion migration or electromigration of the contact materials, as well as electrochemical damage to the active material^{26–29}. In recent years, progress has been achieved in improving the stability of all-inorganic perovskites²⁶. Yet, the instability issue is perpetrating for hybrid perovskites, which are particularly attractive for their versatile and facile solution synthesis and device integration.

We consider the problem of the high-bias stability of perovskites as inherently insurmountable, necessitating the research into low-voltage device concepts. In this work, we focus on using a photovoltaic device, where the only electric field is the one originating from the work-function asymmetry of the used electrical contacts. This notion is supported by the recent advancements in the long-term operational stability of perovskite solar cells³⁰. Considering the high calculated value of the soft X-ray linear absorption coefficient of MAPbI₃ (Extended Data Fig. 1), taking the highest reported $\mu\tau$ values for this material (up to 10⁻² cm² V⁻¹), and a typical build-in potential of 1 V, we estimate that the requirement of simultaneously high charge-collection efficiency (CCE) close to unity along with near-complete X-ray absorption (10–30 keV) can be met by an active layer having a thickness in the range of 50–500 μm . The practical embodiment of such an X-ray photovoltaic (XPV) device is essentially a highly efficient perovskite solar cell with a single-crystalline (SC) absorption layer of several hundred micrometres. The utilization of polycrystalline thick perovskite layers is unacceptable owing to the orders of magnitude lower $\mu\tau$ values due to carrier scattering at the grain boundaries and defects^{31,32}, which proportionally compromises the CCE and necessitates higher applied bias.

Motivated by the recent advances in the solution growth of highly efficient SC perovskite solar cells (~20 μm (refs. 33–36)), we sought to examine several-hundred-micrometre-thick perovskite MAPbI₃ SC XPV devices (Fig. 1a,b). Such an order of magnitude thicker SC layer was directly grown on a conductive substrate by a low-temperature solution method as a single-pixel device and as a two-dimensional (2D) panel and one-dimensional (linear) arrays with high spatial resolution. Although operating in the XPV mode (that is, zero applied bias), the devices exhibit a noise-equivalent dose below one X-ray photon and DE close to unity. Poissonian-photon-statistics-limited X-ray imaging was thus demonstrated, down to extremely low doses of tens of nanogray in air (nGy_{air}). These characteristics are retained for at least a year. Furthermore, energy-resolved X-ray imaging could be demonstrated, discriminating between materials of different compositions, which are otherwise indistinguishable in contrast-only X-ray transmission imaging.

Results

MAPbI₃ SC XPV devices

For obtaining a few-hundred-micrometre-thick MAPbI₃ SC film, a space-confined inverse-temperature crystallization method was adopted and adjusted from other work^{33,37}. The perovskite films were grown on indium tin oxide (ITO) substrates coated with poly(triaryl) amine (PTAA) as a hole-transporting layer, followed by the thermal evaporation of fullerene (C₆₀)/bathocuproine (BCP) layer as the electron-transporting layer and Cu electrode, completing the XPV device (Fig. 1a–c). Contacts with asymmetric work-function potentials for establishing an internal electrical field and good charge selectivity of the transport layers are paramount for the desired XPV operation mode. Nevertheless, the as-obtained thick XPV devices had poor detector performance, which we attribute to the effect of persistent, residual solvates that may form with the specific solvent used (γ -butyrolactone) (ref. 38), trapped in the interfaces between the SC and PTAA layer (Supplementary Fig. 1a). The issue was satisfactorily mitigated with the extensive post-drying of crystals at room temperature in a nitrogen-filled drybox (Supplementary Fig. 1b). Supplementary Fig. 1c illustrates the improvement in X-ray detection performance (expressed in normalized signal-to-noise ratio (SNR) under the same dose rate) with post-conditioning time, which is correlated with the increase in shunt resistance and rise in X-ray photocurrent. The SNR value reaches a saturated value typically in around one month.

Figures of merit of perovskite X-ray detectors

The performance characteristics that are most relevant, practical and can objectively compare perovskite detectors across laboratories need to be discussed first. X-ray sensitivity is by far the most commonplace reported figure of merit in the rapidly growing area of perovskite X-ray detectors, owing to the simplicity of its measurement. Higher sensitivities are achieved by device biasing at higher electrical fields (Extended Data Fig. 2a) and hence at the cost of excessive noise and dramatic degradation in SNR (Supplementary Fig. 2). Unlike conventional semiconductors such as CdTe, lead halide perovskites are mixed electronic–ionic conductors³⁹, further magnifying the electronic and electrochemical instabilities at high bias. Furthermore, emphasizing sensitivity may erroneously motivate research efforts towards photoconductors, as in the latter, the sensitivity can be amplified via photoconductive gain⁴⁰. The latter, however, also increases the noise levels, response time and device instability. This approach is of somewhat limited utility for materials with poor charge transport characteristics (namely, amorphous Se, quantum dots and so on) and, in the case of perovskites, would require imparting imbalanced charge transport by, for instance, the intentional deterioration of material by introducing charge traps. Another characteristic, commonly used for perovskite detectors, is the detection limit of the dose rate^{14,19,41}, which remains a highly ambiguous parameter as it scales with the integration time (Extended Data Fig. 2b). As the resulting detection limit is lower for a higher accumulated dose, the utility of the reported detection limit values is higher when the integration times are specified (Supplementary Notes 1–3).

An overarching objective, foremost in medical imaging, is to attain the desired imaging quality and minimizing the acquired radiation dose. In this regard, the MAPbI₃ SC detector operated in the XPV mode (0 V bias) favourably compares with the state-of-the-art commercial gadolinium oxysulfide (GOS) scintillator detectors in terms of image contrast and image noise, especially when decreasing the dose to as low as 8 nGy_{air} (Fig. 1d and Supplementary Figs. 3 and 4). Quantitatively, the image quality is determined by the SNR, which—for the ideal detector—has the fundamental limit given by Poissonian statistics, that is, the photon shot noise. Denoting n_{ph} as the mean number of X-ray photons incident on the detector, the limit for SNR is $\text{SNR}_{\text{ideal}} = \sqrt{n_{\text{ph}}}$ (ref. 42). Consequently, a well-thought figure of merit is the detective quantum efficiency (DQE) defined via the SNR analysis as

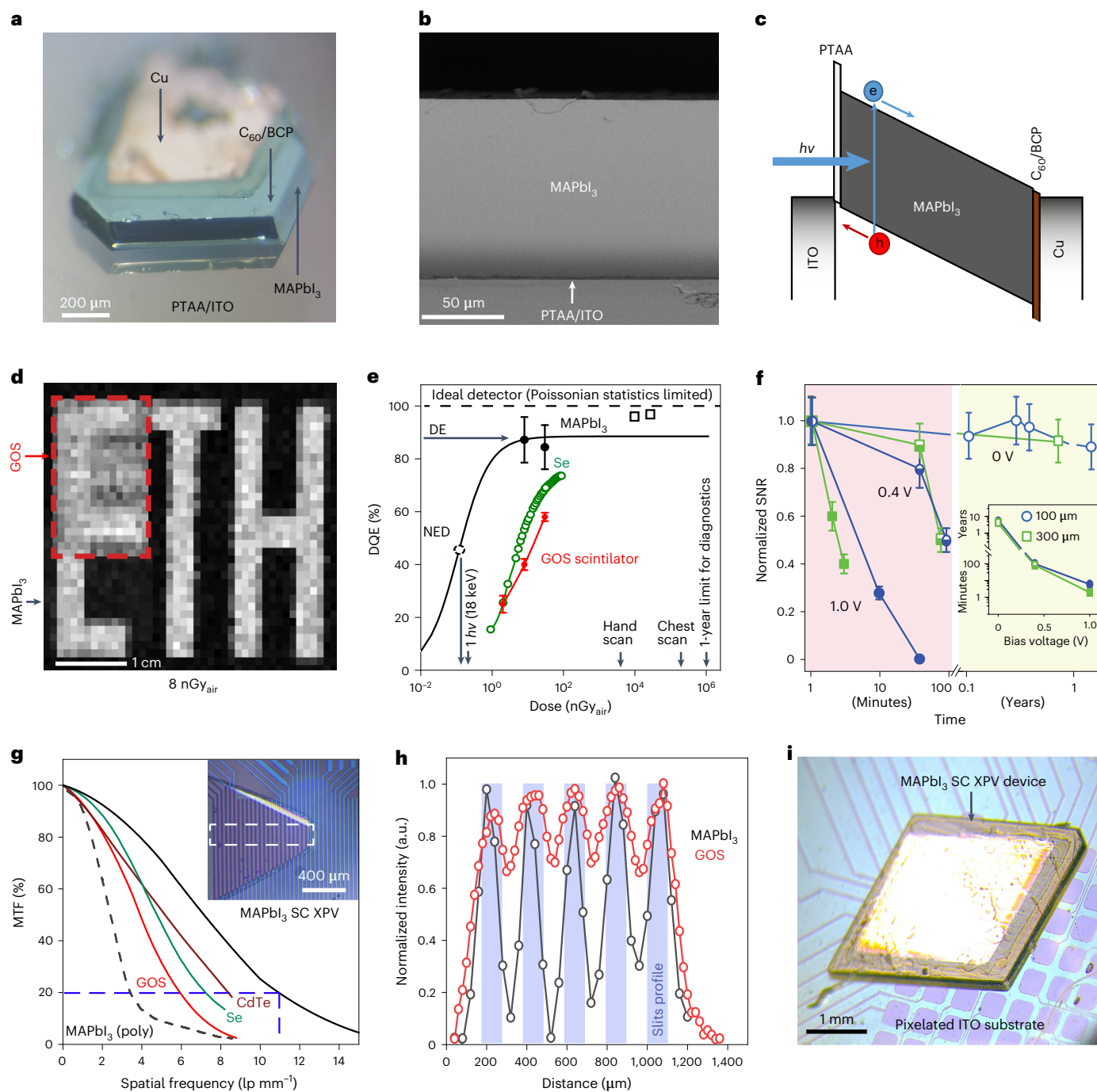


Fig. 1 | MAPbI₃ SC X-ray detector and its figures of merit. a, A 110 μm MAPbI₃ SC XPV device with a description of the layers. Scale bar, 200 μm. **b**, Cross-sectional scanning electron microscopy image of a MAPbI₃ SC grown directly on a PTAA/ITO substrate. Scale bar, 50 μm. **c**, Energy band alignment and operation principle in the XPV mode. **d**, X-ray imaging of a stencil mask (Supplementary Fig. 3) at doses of 8 nGy_{air}. The inset shows imaging with the GOS scintillator detector. Scale bar, 1 cm. **e**, DQE dependencies on the dose. The solid black line and points represent the model and experimental data (calculated from **d** and Supplementary Fig. 4) for MAPbI₃ SC, respectively. The red points are experimental data for the GOS scintillator. The green points are amorphous Se data from another work¹⁵. The black open squares show the calculated DQE for doses at which X-ray imaging was previously demonstrated with MAPbI₃ detectors²⁰. **f**, Normalized SNR dependence versus time for various bias voltages and device thicknesses. The inset shows the estimated half-life dependence on the bias voltage. The data points represent mean values, whereas the error bars

are r.m.s. deviations. They are estimated for 9,600 on/off cycles with a lock-in amplifier (for 960 Hz modulation frequency for X-rays and 10 s integration time). **g**, MTF dependencies versus spatial frequency for MAPbI₃ SC XPV device (solid black line), polycrystalline MAPbI₃ (ref. 13) (dashed black line) and commercial detectors, namely, GOS (ref. 13) (green line), amorphous Se (ref. 13) (red line) and CdTe SC⁵⁴ (brown line). The inset shows the through-bottom view on MAPbI₃ SC directly grown on a linear array of ITO electrodes. The inner part limited by the dashed lines illustrates the opening of a steel mask aperture. Scale bar, 400 μm. **h**, Signal intensity profiles were obtained under 50 kVp X-ray irradiation illuminating the steel stencil mask with 100-μm-wide slits, arranged with a spatial frequency of 5 lp mm⁻¹ (blue lines); the experimental results were measured with a GOS commercial scintillator imager with 20 μm pixel pitch (red) and MAPbI₃ XPV SC linear detector array with 40 μm line pitch (black). **i**, MAPbI₃ XPV device directly grown on a pixelated ITO substrate. Scale bar, 1 mm.

$DQE = SNR(D)_{\text{detector}}^2 / SNR(D)_{\text{ideal}}^2$ as a function of incident dose D (ref. 43). The DQE is commonly used for benchmarking commercial X-ray imagers, regardless of the detector technology (that is, scintillating or direct detection). To represent the DQE as a function of D ($\propto n_{\text{ph}}$), we propose the following model for a single-pixel device (spatial frequency, $\nu = 0$):

$$DQE(\nu = 0, D) = \frac{DE}{1 + \frac{NED}{D}}, \quad (1)$$

where NED is the noise-equivalent dose⁴⁴ and DE is the detection efficiency (Supplementary Note 1 provides the derivation of equation (1)). DE is the fraction of detected photons versus total incoming photons, which is given by an integral for a product of the X-ray attenuation efficiency and CCE over the detector thickness. The NED is such a dose $D(n_{\text{ph}})$ for which the photon shot noise is equal to the intrinsic electric detector noise, the latter comprising thermal noise, charge-carrier shot noise and so on. In the ideal case, a detector should have a DE value of unity and NED much less than the dose of a single photon and hence a dose-independent DQE value approaching unity. Thus, an X-ray dose would be minimized to the theoretical value required to reach the desired SNR, as the latter is only limited by Poissonian photon statistics. Figure 1e compares the DQE versus D values for a commercial direct conversion detector (amorphous Se (ref. 15)) and scintillator (GOS, obtained via SNR analysis of the images), and MAPbI₃ SC operated in the XPV mode (calculated according to equation (1), using the measured values of NED = 90 pGy_{air} and DE = 88%). The DQE values for MAPbI₃ SC were further confirmed by an SNR analysis of the X-ray images at doses of 8 and 32 nGy_{air} (Fig. 1d, Supplementary Fig. 4 and Methods). Noteworthy, a dose of 8 nGy_{air} is around three orders of magnitude lower than the one received by a patient during typical X-ray imaging⁴⁵ or those typically used for X-ray imaging with perovskites^{13,20}. With NED being smaller than one photon, the noise levels need not be further improved for minimizing the accumulated dose for achieving the same X-ray imaging quality.

Owing to the zero-bias operation, these XPV devices retain their characteristics for at least one and a half year (in air, without encapsulation), with the projected device half-life (time that corresponds to a 50% drop in the normalized SNR) of several years. On the contrary, complete degradation occurs within a few hours at high applied electric fields (Fig. 1f). The operational stability of XPV devices, thus, reaches the typical chemical shelf-life of MAPbI₃ SC, despite the relatively high dose accumulated during these tests (6 mGy, equivalent to ~500 conventional X-ray medical scans). Additionally, the radiation hardness was tested as an X-ray photocurrent stability under the dose rate of 1 Gy_{air} min⁻¹ for 14 h, resulting in an accumulated high dose of 850 Gy_{air} (equivalent to 80,000 computed tomography scans of the chest), without any notable deterioration in the photocurrent (Supplementary Fig. 5).

Using the advantages of solution-grown synthesis, MAPbI₃ SC XPV was directly fabricated on conductive substrates patterned in the form of linear and 2D panel array detectors (Fig. 1g–i, Supplementary Fig. 6 and Extended Data Fig. 3). To estimate the spatial resolution, modulation transfer function (MTF) dependence on the spatial resolution was evaluated and compared with previously reported polycrystalline MAPbI₃ device and commercial detectors (Fig. 1g). The MTF reaches 20% for the spatial frequency of 11 lp mm⁻¹ for the linear detector array with a 40 μm pixel pitch, which is superior to the state-of-the-art commercial detector materials, and is so far the highest spatial resolution for perovskite X-ray direct detectors, to the best of our knowledge. This is confirmed with the X-ray intensity profile of 100 μm slits with a spatial frequency of 5 lp mm⁻¹, where the profile obtained with MAPbI₃ is evidently sharper than that obtained with the GOS scintillator (Fig. 1h). Additionally, the high-resolution X-ray image is obtained, where features with a size down to 100 μm are effectively

resolvable (Supplementary Fig. 7). MTF dependencies on a spatial frequency normalized on the pixel pitch (in units of Nyquist frequency fraction) are shown in Extended Data Fig. 4, where a notable divergence from the theoretical prediction is evident for the 40-μm-pitch MAPbI₃ XPV device. This indicates that the spatial resolution is approaching the limit given by the size of the X-ray-generated charge cloud, which is evaluated in the next section. Based on the estimated MTF values and as per another work⁴⁶, DQE as a function of spatial frequency is evaluated (Extended Data Fig. 5), emphasizing that the DQE values are higher than 50% for spatial frequencies up to 5 lp mm⁻¹.

In the following, we further detail the rationale and experimental path to attain such high X-ray detection characteristics of the MAPbI₃ SC detector.

DE and charge transport properties

The highest DE values are expected in the SC thickness range of 50–220 μm, where the experimentally obtained CCE and X-ray attenuation efficiency, computed from the database values⁴⁷, are high (Extended Data Fig. 6). High efficiency of photovoltaic devices with a thickness of up to 220 μm is additionally verified with the J – V characteristic under one-sun illumination (Supplementary Fig. 8), showing only a minor change in the short-circuit current and open-circuit voltage. Comparing the simulated⁴⁸ and measured J – V characteristics (Supplementary Fig. 8), the surface trap density of the fabricated XPV MAPbI₃ SC devices is evaluated to be in the range of 10¹⁶–10¹⁷ cm⁻³. We also note that a further decrease in the surface defect density does not evidently increase the short-circuit current and thus the CCE, but moderately affects the open-circuit voltage and hence is more relevant for solar cells³⁴. For the simplest case, namely, a single kind of charge carrier originating from the absorption of photons by the device surface, CCE can be expressed with the Hecht equation⁴⁹ as

$$CCE = \frac{L_d}{d} \left(1 - \exp\left(-\frac{d}{L_d}\right) \right), \quad (2)$$

where d is the drift distance (equal to the device thickness) of a charge to the corresponding electrode, $L_d = \mu\tau E$ is the charge-carrier drift length, E is the electrical field ($E = U/d$ and U is the electrical potential). Another work⁵⁰ developed a model for the CCE (and DE) under X-ray exposure, where the Hecht equation is modified to account for the penetration depth of X-rays and hence a volumetric distribution of generated charges, as well as the asymmetry of transport properties for electrons and holes. We first use this model to assess the expected performances of XPV devices with the given charge transport properties and in relation to the SC thickness and then compare with the experimental CCE and DE values. In the XPV mode, the electrical-field strength E is fully defined by the build-in potential U , that is, the open-circuit voltage $V_{\text{oc}} = 1.1$ V under one-sun illumination conditions (Fig. 2a), which was additionally confirmed with the photocurrent dependence on the bias voltage under X-ray irradiation (Extended Data Fig. 7a). The estimation of $\mu\tau$ values is, however, somewhat ambiguous. Their lower limit ($\mu_e\tau_{\text{min}} = 6 \times 10^{-4}$ cm² V⁻¹ and $\mu_h\tau_{\text{min}} = 2 \times 10^{-4}$ cm² V⁻¹) was estimated by separately measuring the mobility of each carrier type using the time-of-flight (ToF) technique⁵¹ (Fig. 2b,c and Supplementary Fig. 9) and multiplying these values by their mean lifetime estimated from the transient photocurrent response ($\tau \geq 6$ μs; Supplementary Fig. 10). The measured charge carriers' mobility (91 cm² V⁻¹ s⁻¹ for electrons and 31 cm² V⁻¹ s⁻¹ for holes) is an order of magnitude higher than the typical values reported in polycrystalline perovskite thin films¹², owing to the lower trap density. The upper $\mu\tau$ limit for the majority carrier ($\mu_e\tau_{\text{max}} = 3 \times 10^{-3}$ cm² V⁻¹) was directly obtained as a fitting parameter (in the Hecht equation) of photocurrent versus bias voltage dependence (Extended Data Fig. 7b). For the devices illuminated from the side of the hole-collecting electrode, $\mu_e\tau$ values set the CCE dependence on the detector thickness, being in good agreement with the experiment

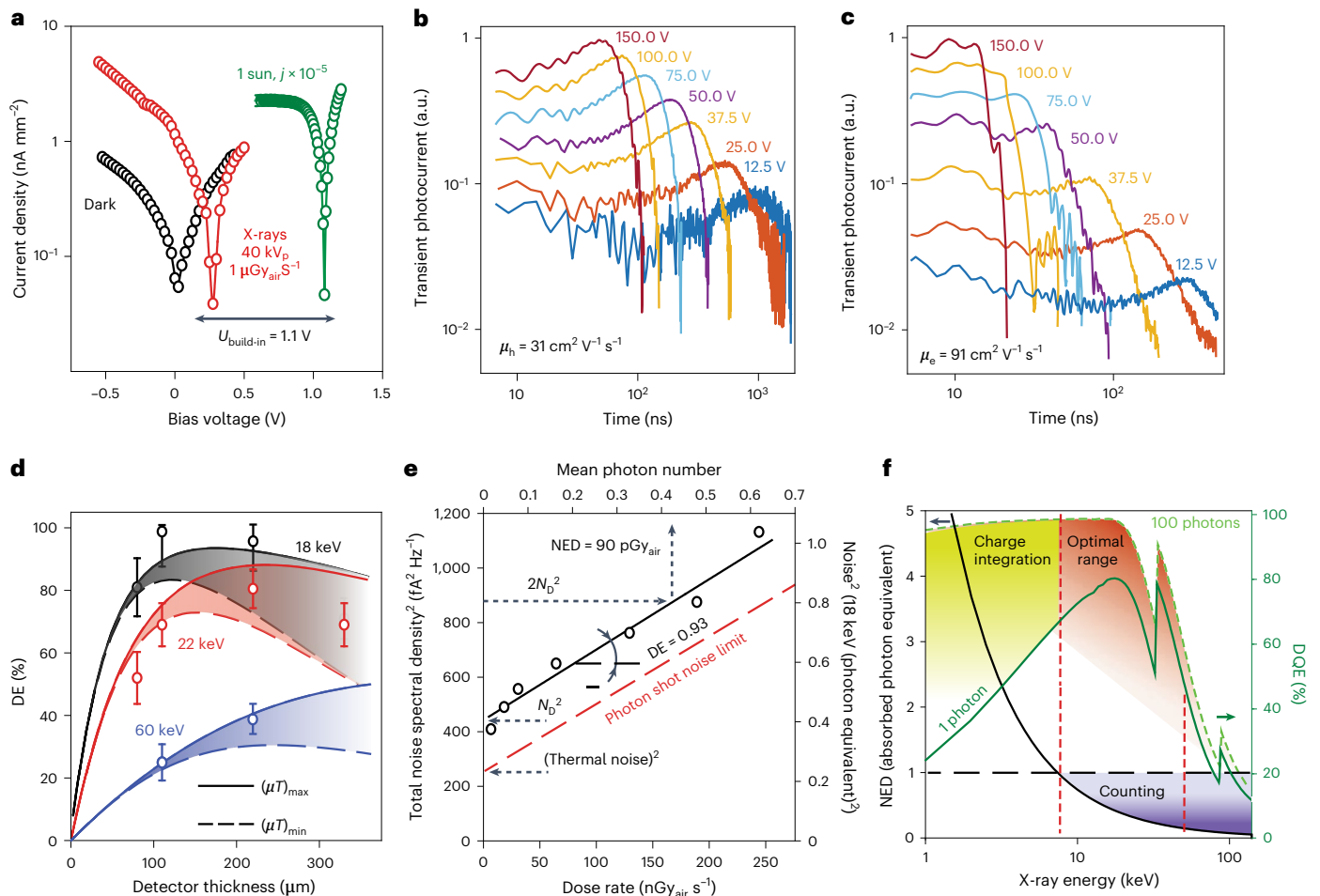


Fig. 2 | Charge transport and X-ray detection performance of MAPbI₃ SC XPV detectors. **a**, I - V curves in the dark and under X-ray and light illumination, used to estimate the build-in potential of ~ 1.1 V. **b**, **c**, ToF traces for holes (**b**) and electrons (**c**) under blue laser pulses for various bias voltages, used to determine the charge carrier mobility. **d**, X-ray DE dependence on thickness for different X-ray photon energies (shown in different colours), calculated based on models (lines) with upper (solid) and lower (dashed) limits of $\mu\tau$ evaluation. The open circles represent the experimental DE data. The data points represent the mean values and the error bars are r.m.s. deviations. They are estimated for 9,600 on/off cycles with a lock-in amplifier (for 960 Hz modulation frequency of X-rays and 10 s integration time), accounting for the error in dose rate measurements and

accuracy of detector area estimation. **e**, Squared-noise-current spectral density dependence on the dose rate together with N_T^2 , expressed in photon equivalents, depending on the mean photon number over an integration time of 500 μ s (the black circles are experimental data and the black line is the fit with equation (3)). **f**, NED (black line) and DQE (green lines) versus photon energy, calculated from the experimental DE and NED; DQE is shown for a single photon (solid line) and 100 photons (dashed line); the energy ranges where only the charge-integration regime is possible and the photon-counting regime becomes allowed are highlighted in yellow and blue, respectively. The optimal energy range is shaded in red.

(Supplementary Fig. 11a,b). Then, the thickness-dependent DE is calculated for both limits, combining photon-energy-dependent X-ray attenuation efficiency and the CCE, as well as accounting for ambipolar charge transport. For $\mu\tau_{\max}$, we take a value of 30% of $\mu_e\tau_{\max}$, considering the μ_e/μ_h ratio measured using the ToF. The calculated DE values are in good agreement with the experimental data (Fig. 2d). In particular, the DE of the 220- μ m-thick device is mostly limited by X-ray attenuation efficiency, and reaches 80% for 22 keV X-ray radiation, whereas at thicknesses larger than 220 μ m, the DE becomes limited by the CCE. The charge drift length ($L_d = \mu\tau V_{oc}d^{-1}$) remains very high even for 200- μ m-thick crystals (Supplementary Fig. 11a), allowing to simultaneously reach a CCE value of $\sim 100\%$ and high X-ray absorption (80% at 40 keV).

The theoretical limit of the spatial resolution is mainly defined by the diffusive spreading of the X-ray-generated charge cloud in devices with a moderate electric field (XPV mode). The latter is evaluated as the charge-carrier diffusion length $L_{dif} = \sqrt{\mu\tau kT e^{-1}}$, where k is the Boltzmann constant, T is the temperature and e is the elementary

charge. For electrons, the diffusion length is equal to ~ 40 μ m, agreeing well with the dependence of spatial resolution on pixel density (Supplementary Fig. 12a), which becomes nonlinear at a density greater than 10 pixels per mm (that is, a pixel pitch of 100 μ m). Consequently, MTF growth becomes slower than expected with a further decrease in pitch size (Supplementary Fig. 12b).

Assessing noise and DQE

Although DE is sufficient to describe the detector signal, NED is the comprehensive descriptor for the noise of a detector. To estimate the NED, the X-ray dose-rate-dependent total noise (N_T) of the MAPbI₃ SC detector was obtained as the noise-current spectral density (Fig. 2e and Extended Data Fig. 8). Also, N_T^2 is expressed in photon-equivalent units, where a single-photon equivalent is the root mean square (r.m.s.) of the noise charge equal to the charge generated by one photon in time window t (equal to 500 μ s, given by the amplifier bandwidth of 1 kHz; Fig. 2e, right). In Fig. 2e, the dose rate is recalculated to an equivalent photon quantity within t . The dependence of N_T^2 versus n_{ph} is a linear

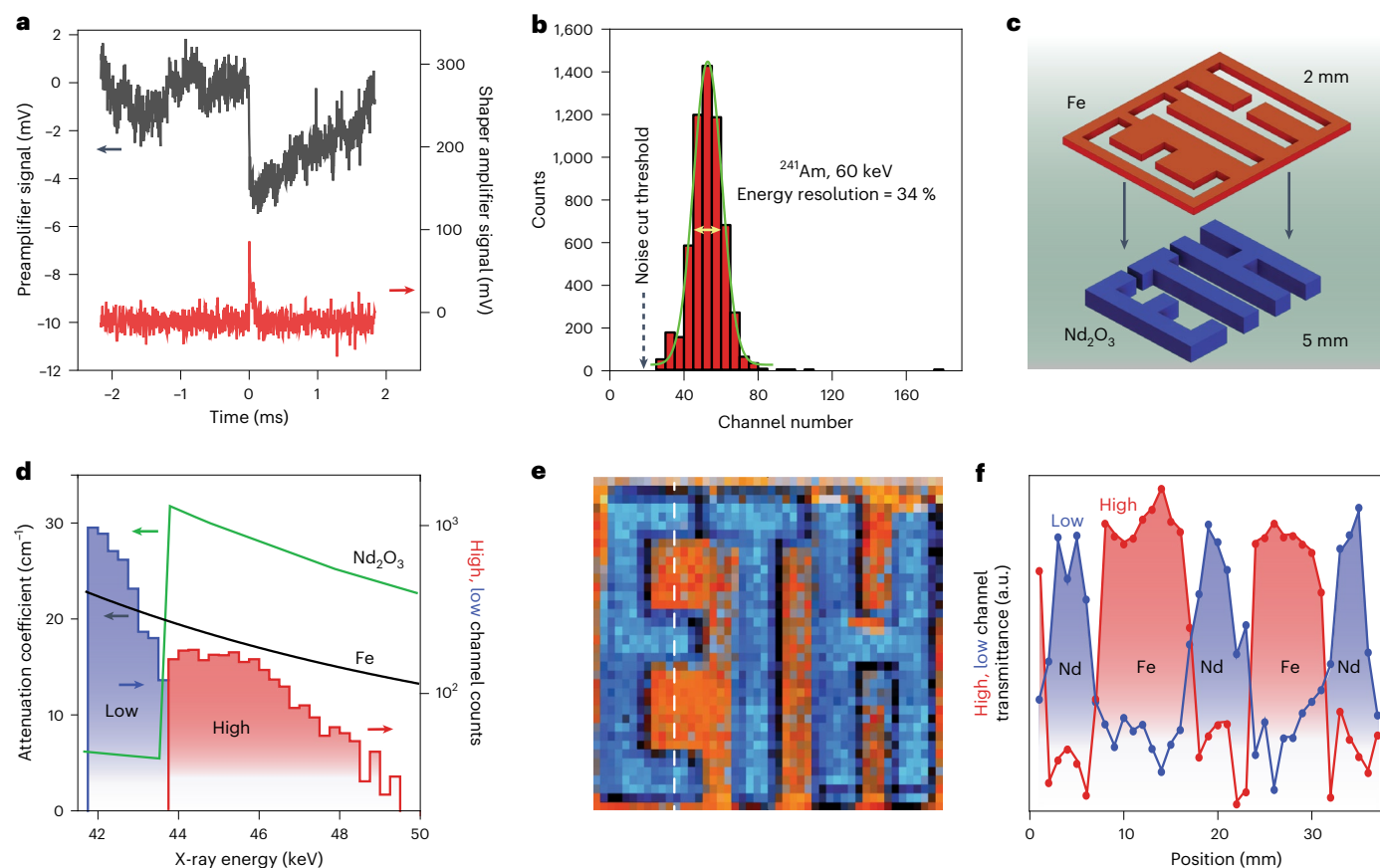


Fig. 3 | X-ray energy-resolved imaging. **a**, γ -ray single-photon counting. An event from ^{241}Am radiation source ($E_\gamma = 60$ keV) was recorded with a MAPbI₃ SC (thickness, 110 μm ; 0 V bias). The black curve is a trace from the charge-integrating preamplifier, and the red curve is the corresponding trace from the shaping amplifier. **b**, Energy-resolved spectrum of 60 keV photons from a radioactive ^{241}Am source. **c**, The imaged object is a rectangle comprising two complementary patterns: 5-mm-thick ETH letters made of Nd_2O_3 powder surrounded by a 2-mm-thick steel frame. **d**, Attenuation coefficients versus X-ray photon energy for Fe (black curve) and Nd_2O_3 (green curve) shown on top of an

example of 50 kV_p energy spectrum transmitted through the Nd part of the object recorded by the MAPbI₃ SC detector. The spectrum was binned into low-energy (blue) and high-energy (red) channels, with a border that corresponds to the characteristic K line of Nd. **e**, Energy-resolved X-ray imaging of the object from **c** under 50 kV_p X-ray irradiation with the MAPbI₃ SC detector, where the colours denote the transmittance for the corresponding two energy channels from **d**. **f**, Transmittance of low-energy (blue) and high-energy (red) channels along the white dashed line in **e**.

function with a slope of DE and an offset of the square of the detector noise (N_D^2) (Supplementary Note 2):

$$N_T^2 \left[(\text{photon equivalent})^2 \right] = \text{DE} \times n_{\text{ph}} + N_D^2. \quad (3)$$

The red line in Fig. 2e shows the theoretical limit for the sum of photon shot noise and thermal noise. A fit of the experimental data with equation (3) gives DE = 0.93, in good agreement with the DE estimated from the CCE and X-ray attenuation efficiency (Fig. 2d). The experimental detector noise exceeds the fundamental lowest limit by only 30%, which is given by the thermal noise⁵², calculated based on the device resistance. Such a low detector noise emphasizes the absence of dark-current-induced electron shot noise and the negligible effects of ionic diffusivity in the XPV mode. NED was then calculated as the offset/slope ratio in equation (3) (ref. 44) and amounted to -0.4 photon equivalents at 18 keV, which corresponds to a dose of -90 pGy_{air} for a 0.8 mm² detector area.

NED versus X-ray energy plot allows the estimation of the energy onset for the photon-counting regime (for instance, -7 keV for 110- and 220- μm -thick devices; Fig. 2f). At lower photon energies (with higher flux), the charge-integration mode is used instead and DQE begins to decline with a further increase in photon energies as the X-ray

attenuation efficiency drops (Fig. 2f, 220- μm -thick device; Supplementary Fig. 13, 110- μm -thick device; Supplementary Note 4 provides details of the calculation of NED and DQE dependence on energy), defining the ranges of -10–25 keV (110- μm -thick device) and -10–50 keV (220- μm -thick device) as optimal for X-ray imaging at low doses and mostly limited by the photon shot noise (Fig. 1d and Supplementary Fig. 4). In this energy range, the DQE reaches 60%–90% on absorption of just a dozen photons by the device (within the integration time window; Supplementary Fig. 14a, 110- μm -thick device; Supplementary Fig. 14b, 220- μm -thick device)

X-ray energy-resolved imaging

Single-photon detection capability directly stems from the NED being below one photon equivalent; examples of the obtained single-photon signal traces with different types of preamplifier are provided in Fig. 3a and Supplementary Fig. 15. The maximum counting rate reaches 10^7 photons $\text{s}^{-1} \text{mm}^{-2}$ at 100 μm pitch size (Supplementary Fig. 16), which is suitable for application in mammography. A further decrease in pitch size below the X-ray photon-generated charge cloud size (-100 μm for our case) will hinder the photon-counting efficiency and X-ray energy resolution due to charge sharing between the neighbouring pixels. Low-noise and high-charge-collection characteristics allow single-photon counting from ^{241}Am source (60 keV)

with an energy resolution of ~34% (Fig. 3b). Although the obtained energy resolution is not suitable for applications in high-resolution γ -spectroscopy, it is feasible for energy-discriminated X-ray spectral imaging, the so-called X-ray dual-colour imaging⁵³ at moderate count rates, reaching limits required by digital mammography. As a showcase, we used a several-millimetre-thick rectangular object consisting of two complementary 'ETH' patterns made of two different materials with different X-ray attenuation versus X-ray energy dependencies (Fe and Nd₂O₃; Fig. 3c). Specifically, compared with Fe, the X-ray attenuation coefficient of Nd is much lower than 43 keV and much higher above this value (due to its K atomic shell; Fig. 3d). The thicknesses of each pattern were adjusted for attaining minimal overall X-ray transmission contrast; the letters are then somewhat readable only due to X-ray shadowing when imaging at a non-orthogonal angle to the X-ray tube (Supplementary Fig. 17). One can readily distinguish between the two materials and obtain a high-contrast image when recording the images using a low-energy channel (more attenuated by Fe) or high-energy channel (more suppressed by Nd), as indicated by the red and blue regions, respectively (Fig. 3e,f).

Discussion

In conclusion, MAPbI₃ SC X-ray detectors operated in the photovoltaic mode are shown to exhibit long-term stable and high X-ray detection performance in the soft X-ray range (20–50 keV), with DQE of ~87% at a low dose of 8 nGy_{air}, NED of ~90 pGy_{air} and DE of up to 88% at a spatial resolution of 11 lp mm⁻¹ (corresponding to MTF = 20%). The compelling aspects of the hybrid perovskite SC XPV technology are summarized in Extended Data Table 1. A comparison with existing radiation detection materials in terms of basic materials properties and state-of-the-art device characteristics is shown in Supplementary Table 1. Our findings attest to the suitability of hybrid lead halide perovskites—when operated in the photovoltaic mode—as a practical low-cost detector technology for medical X-ray imaging such as mammography and radiography, where high SNR at a low dose is crucial and hence motivate future work on the commercial implementation of perovskite-based XPV array detectors.

Online content

Any methods, additional references, Nature Portfolio reporting summaries, source data, extended data, supplementary information, acknowledgements, peer review information; details of author contributions and competing interests; and statements of data and code availability are available at <https://doi.org/10.1038/s41566-023-01207-y>.

References

- Locker, M. et al. Single photon counting X-ray imaging with Si and CdTe single chip pixel detectors and multichip pixel modules. *IEEE Trans. Nucl. Sci.* **51**, 1717–1723 (2004).
- Brombal, L. et al. Large-area single-photon-counting CdTe detector for synchrotron radiation computed tomography: a dedicated pre-processing procedure. *J. Synchrotron Rad.* **25**, 1068–1077 (2018).
- Milbrath, B. D., Peurrung, A. J., Bliss, M. & Weber, W. J. Radiation detector materials: an overview. *J. Mater. Res.* **23**, 2561–2581 (2008).
- Yakunin, S. et al. Detection of gamma photons using solution-grown single crystals of hybrid lead halide perovskites. *Nat. Photon.* **10**, 585–589 (2016).
- Wang, P. L. et al. Hard radiation detection from the selenophosphate Pb₂P₂Se₆. *Adv. Funct. Mater.* **25**, 4874–4881 (2015).
- Stoumpos, C. C. et al. Crystal growth of the perovskite semiconductor CsPbBr₃: a new material for high-energy radiation detection. *Cryst. Growth Des.* **13**, 2722–2727 (2013).
- Androulakis, J. et al. Dimensional reduction: a design tool for new radiation detection materials. *Adv. Mater.* **23**, 4163–4167 (2011).
- Abbaspour, S., Mahmoudian, B. & Islamian, J. Cadmium telluride semiconductor detector for improved spatial and energy resolution radioisotopic imaging. *World J. Nucl. Med.* **16**, 101–107 (2017).
- Fiederle, M., Procz, S., Hamann, E., Fauler, A. & Fröjd, C. Overview of GaAs and CdTe pixel detectors using Medipix electronics. *Cryst. Res. Technol.* **55**, 2000021 (2020).
- Zhou, Y., Chen, J., Bakr, O. M. & Mohammed, O. F. Metal halide perovskites for X-ray imaging scintillators and detectors. *ACS Energy Lett.* **6**, 739–768 (2021).
- Sytnyk, M., Deumel, S., Tedde, S. F., Matt, G. J. & Heiss, W. A perspective on the bright future of metal halide perovskites for X-ray detection. *Appl. Phys. Lett.* **115**, 190501 (2019).
- Yakunin, S. et al. Detection of X-ray photons by solution-processed lead halide perovskites. *Nat. Photon.* **9**, 444–449 (2015).
- Kim, Y. C. et al. Printable organometallic perovskite enables large-area, low-dose X-ray imaging. *Nature* **550**, 87–91 (2017).
- Pan, W. et al. Cs₂AgBiBr₆ single-crystal X-ray detectors with a low detection limit. *Nat. Photon.* **11**, 726–732 (2017).
- Panneerselvam, D. M. & Kabir, M. Z. Evaluation of organic perovskite photoconductors for direct conversion X-ray imaging detectors. *J. Mater. Sci. Mater. Electron.* **28**, 7083–7090 (2017).
- Shrestha, S. et al. High-performance direct conversion X-ray detectors based on sintered hybrid lead triiodide perovskite wafers. *Nat. Photon.* **11**, 436–440 (2017).
- He, Y. et al. Resolving the energy of γ -ray photons with MAPbI₃ single crystals. *ACS Photon.* **5**, 4132–4138 (2018).
- Matt, G. J. et al. Sensitive direct converting X-ray detectors utilizing crystalline CsPbBr₃ perovskite films fabricated via scalable melt processing. *Adv. Mater. Interfaces* **7**, 1901575 (2020).
- Tie, S. et al. Robust fabrication of hybrid lead-free perovskite pellets for stable X-ray detectors with low detection limit. *Adv. Mater.* **32**, 2001981 (2020).
- Zhao, J. et al. Perovskite-filled membranes for flexible and large-area direct-conversion X-ray detector arrays. *Nat. Photon.* **14**, 612–617 (2020).
- He, Y. et al. CsPbBr₃ perovskite detectors with 1.4% energy resolution for high-energy γ -rays. *Nat. Photon.* **15**, 36–42 (2021).
- Liu, Y. et al. Ligand assisted growth of perovskite single crystals with low defect density. *Nat. Commun.* **12**, 1686 (2021).
- Deumel, S. et al. High-sensitivity high-resolution X-ray imaging with soft-sintered metal halide perovskites. *Nat. Electron.* **4**, 681–688 (2021).
- Wei, H. et al. Dopant compensation in alloyed CH₃NH₃PbBr_{3-x}Cl_x perovskite single crystals for gamma-ray spectroscopy. *Nat. Mater.* **16**, 826–833 (2017).
- He, Y. et al. Demonstration of energy-resolved γ -ray detection at room temperature by the CsPbCl₃ perovskite semiconductor. *J. Am. Chem. Soc.* **143**, 2068–2077 (2021).
- Hui, Y. et al. Stability of perovskite thin films under working condition: bias-dependent degradation and grain boundary effects. *Adv. Funct. Mater.* **31**, 2103894 (2021).
- Futscher, M. H. et al. Quantification of ion migration in CH₃NH₃PbI₃ perovskite solar cells by transient capacitance measurements. *Mater. Horiz.* **6**, 1497–1503 (2019).
- Khenkin, M. V., K. M. A., Katz, E. A. & Visoly-Fisher, I. Bias-dependent degradation of various solar cells: lessons for stability of perovskite photovoltaics. *Energy Environ. Sci.* **12**, 550–558 (2019).
- Domanski, K. et al. Not all that glitters is gold: metal-migration-induced degradation in perovskite solar cells. *ACS Nano* **10**, 6306–6314 (2016).
- Jeong, J. et al. Pseudo-halide anion engineering for α -FAPbI₃ perovskite solar cells. *Nature* **592**, 381–385 (2021).

31. Datta, A., Zhong, Z. & Motakef, S. A new generation of direct X-ray detectors for medical and synchrotron imaging applications. *Sci. Rep.* **10**, 20097 (2020).
32. Peng, J. et al. X-ray detection based on crushed perovskite crystal/polymer composites. *Sens. Actuator A Phys.* **312**, 112132 (2020).
33. Chen, Z. et al. Single-crystal MAPb₃ perovskite solar cells exceeding 21% power conversion efficiency. *ACS Energy Lett.* **4**, 1258–1259 (2019).
34. Alsalloum, A. Y. et al. Low-temperature crystallization enables 21.9% efficient single-crystal MAPb₃ inverted perovskite solar cells. *ACS Energy Lett.* **5**, 657–662 (2020).
35. Alsalloum, A. Y. et al. 22.8%-efficient single-crystal mixed-cation inverted perovskite solar cells with a near-optimal bandgap. *Energy Environ. Sci.* **14**, 2263–2268 (2021).
36. Efros, A. L. & Karpov, V. G. Electric power and current collection in semiconductor devices with suppressed electron–hole recombination. *ACS Energy Lett.* **7**, 3557–3563 (2022).
37. Saidaminov, M. I. et al. High-quality bulk hybrid perovskite single crystals within minutes by inverse temperature crystallization. *Nat. Commun.* **6**, 7586 (2015).
38. Fateev, S. A. et al. Solution processing of methylammonium lead iodide perovskite from γ -butyrolactone: crystallization mediated by solvation equilibrium. *Chem. Mater.* **30**, 5237–5244 (2018).
39. Tress, W. Metal halide perovskites as mixed electronic–ionic conductors: challenges and opportunities—from hysteresis to memristivity. *J. Phys. Chem. Lett.* **8**, 3106–3114 (2017).
40. Neamen, D. A. *Semiconductor Physics and Devices: Basic Principles* 4th edn, 633–635 (McGraw-Hill, 2012).
41. Pan, L., Shrestha, S., Taylor, N., Nie, W. & Cao, L. R. Determination of X-ray detection limit and applications in perovskite X-ray detectors. *Nat. Commun.* **12**, 5258 (2021).
42. Berger, M., Yang, Q. & Maier, A. *Medical Imaging Systems* 136–139 (Springer, 2018).
43. Zanella, G. & Zannoni, R. The role of the quantum efficiency on the DQE of an imaging detector. *Nucl. Instrum. Meth. Phys. Res. A* **381**, 157–160 (1996).
44. Isaias, D. J., Sarah, J. B., Michael, J. P. & Kungang, Z. A comparison of quantum limited dose and noise equivalent dose. In *Proc. SPIE 9783, Medical Imaging 2016: Physics of Medical Imaging* 97833T (SPIE, 2016).
45. Mettler, F. A., Huda, W., Yoshizumi, T. T. & Mahesh, M. Effective doses in radiology and diagnostic nuclear medicine: a catalog. *Radiology* **248**, 254–263 (2008).
46. McMullan, G. et al. Electron imaging with Medipix2 hybrid pixel detector. *Ultramicroscopy* **107**, 401–413 (2007).
47. Berger, M. J. et al. *XCOM: Photon Cross Sections Database* (2013); <https://www.nist.gov/pml/xcom-photon-cross-sections-database>
48. Turedi, B. et al. Perovskite single-crystal solar cells: going forward. *ACS Energy Lett.* **6**, 631–642 (2021).
49. Cho, H. Y., Lee, J. H., Kwon, Y. K., Moon, J. Y. & Lee, C. S. Measurement of the drift mobilities and the mobility-lifetime products of charge carriers in a CdZnTe crystal by using a transient pulse technique. *J. Instrum.* **6**, C01025 (2011).
50. Zahangir Kabir, M. & Kasap, S. O. Sensitivity of X-ray photoconductors: charge trapping and absorption-limited universal sensitivity curves. *J. Vac. Sci. Technol. A* **20**, 1082–1086 (2002).
51. Shrestha, S. et al. Assessing temperature dependence of drift mobility in methylammonium lead iodide perovskite single crystals. *J. Phys. Chem. C* **122**, 5935–5939 (2018).
52. Johnson, J. B. Thermal agitation of electricity in conductors. *Phys. Rev.* **32**, 97–109 (1928).
53. Moghiseh, M. et al. Discrimination of multiple high-Z materials by multi-energy spectral CT—a phantom study. *JSM Biomed. Imaging Data Pap.* **3**, 1007 (2016).
54. Murer, D. Photon counting X-ray detectors for applications in inspection and non-destructive testing. In *AIDA 2020* (2018).

Publisher's note Springer Nature remains neutral with regard to jurisdictional claims in published maps and institutional affiliations.

Open Access This article is licensed under a Creative Commons Attribution 4.0 International License, which permits use, sharing, adaptation, distribution and reproduction in any medium or format, as long as you give appropriate credit to the original author(s) and the source, provide a link to the Creative Commons license, and indicate if changes were made. The images or other third party material in this article are included in the article's Creative Commons license, unless indicated otherwise in a credit line to the material. If material is not included in the article's Creative Commons license and your intended use is not permitted by statutory regulation or exceeds the permitted use, you will need to obtain permission directly from the copyright holder. To view a copy of this license, visit <http://creativecommons.org/licenses/by/4.0/>.

© The Author(s) 2023

Methods

Reagents

γ -Butyrolactone (>99.00%), toluene (anhydrous, 99.80%), C_{60} (98.00%), BCP (99.99%) and octadecyltrichlorosilane (OTS) were purchased from Sigma-Aldrich. Methylammonium iodide was purchased from Greatcell Solar. Lead (II) iodide (ultradry beads; 99.999%) was purchased from Alfa Aesar. PTAA (>99%, Sublimed) was purchased from Xi'an Polymer Light Technology. All the reagents were used as received.

Preparation of substrates for SC growth

ITO substrates with an area of $5 \times 5 \text{ cm}^2$ (8–15 Ω , Delta Technologies) were sequentially cleaned by sonication in soap, deionized water, acetone and isopropanol, followed by ultraviolet–ozone surface treatment for 10 min. Next, the PTAA solution (2.5 mg ml^{-1} in toluene) was spin coated for 30 s at 4,000 rpm, and subsequently annealed at 100 °C for 10 min.

Growth of MAPbI_3 SC

The crystal growth is modified from the previous reports^{33,34}. Briefly, 1.55 M of methylammonium iodide and lead (II) iodide were dissolved in γ -butyrolactone at 60 °C by stirring overnight. Then, 50–750 μl of the solution was placed on a prepared substrate with a spacer (thickness, 20–300 μm) preheated to the solution temperature and enclosed by another PTAA-coated substrate. To induce nucleation and to promote growth, the hotplate was gradually heated to 130 °C at a rate of 2 °C h^{-1} . After the crystallization was finished, the substrates were separated and the remnant solution was quickly cleaned with Kimwipes. The substrates were allowed to slowly cool to room temperature on the hotplate to ensure good electrical and mechanical contact between the substrate and thin SCs. All the procedures other than substrate cleaning were carried out in a nitrogen atmosphere.

MAPbI_3 SC growth on patterned conductive substrates

Substrates, patterned in the form of linear or 2D pixel arrays, were fabricated by photolithography from a fully covered ITO substrate. The ITO substrates (Zhuhai Kaivo Optoelectronic Technology) were sequentially cleaned with anisole, isopropanol and oxygen plasma for 3, 3 and 2 min, respectively. Then, photoresist AZ1518 was spin coated on a substrate at 500 rpm for 5 s and 5,000 rpm for 60 s, followed by baking at 115 °C for 2 min on a hotplate. Next, patterns were written into the samples by exposure to 375 nm ultraviolet light using direct laser writing (Heidelberg Instruments, DWL66+) and development in AZ400K:H₂O (1:4) for 2 min. The samples were baked at 120 °C for another 4 min before being ashed by O₂ plasma for 1 min. Finally, the patterns were etched onto the ITO film (100 nm thick) by wet etching with HCl (37%) for 6 min. For MAPbI_3 SC growth on patterned substrates, two patterned substrates were analogously prepared to continuous ITO substrates. Briefly, the patterned substrates were coated with PTAA and the perovskite solution was enclosed by two PTAA-coated patterned substrates. A 100 μm spacer was used for crystal growth on the patterned substrates. To induce nucleation and to promote growth, the hotplate was gradually heated to 130 °C at a rate of 2 °C h^{-1} . Only the crystals grown on the pixelated area were selected for further electrode deposition and characterization. Three types of device were fabricated (Fig. 1g (inset), Fig. 1i and Extended Data Fig. 3) at different pixel pitch sizes (40, 120 and 500 μm) and contact configuration (one and two dimensions). A total of 14 array devices were fabricated. Common electrode contact deposition was done similar to the single-pixel device, as described below.

Device fabrication

C_{60} (20 nm) and BCP (3 nm) were thermally evaporated without an evaporation mask at a rate of 0.1 $\text{\AA} \text{ s}^{-1}$ on top of the crystals. Then, Kapton tapes were used to form an evaporation mask for Cu electrode (thickness, 80 nm) on the edge of the SCs to avoid short-circuiting. When not specifically mentioned, all further described measurements

were conducted with MAPbI_3 SC XPV devices with the electrode structure shown in Fig. 1c.

Device fabrication for ToF measurement

First, the ITO substrates were treated with an OTS-based self-assembled monolayer and ensured that the surface was insulating and hydrophobic. Then, 1 mM OTS solution bath in isopropanol was prepared and the ITO substrates were dipped inside for 10 min. Later, the substrates were washed with fresh isopropanol to remove the excess absorbed OTS.

The perovskite single crystals were grown on the self-assembled-monolayer-treated substrates using the same crystallization technique to fabricate the XPV devices. After crystal growth, the devices are completed with Cu evaporation.

CCE was estimated to be equivalent to the internal quantum efficiency (considering the corresponding travel distance of charge carriers), measured using a QEX10 spectral response measurement system (PV Measurements), calibrated against a reference silicon photodiode.

Scanning electron microscopy images were obtained using a Teneo VS instrument (Thermo Fisher Scientific). The thicknesses of the crystals were measured by using a profilometer (KLA-Tencor P-7 Stylus).

The ToF method was used for the measurement of the drift velocity of photoexcited charge carriers under an applied electric field. The ToF experiment was performed in the differential mode, where the total number of photoexcited charge carriers is maintained sufficiently below the total charge on the electrodes of SC and the RC time constant of the ToF apparatus is below the transit time of the charge carriers. Photoexcitation is applied through the ITO glass substrate with a diode laser from Becker & Hickl (model BDL-488-SMN; wavelength, 488 nm; pulse duration, about 40 ps). To prevent field-induced polarization (that is, accumulation of ions at the electrodes), the bias is applied as a pulse train of alternating polarity from ± 20 to ± 150 V at a frequency of 150 Hz from an HP 8116A function generator via Falco Systems WMA-300 high-voltage amplifier. Drift time τ is inversely proportional to drift mobility μ and is given by $\mu = d^2/(\tau V)$, where d is the drift distance, τ is the drift time and V is the applied bias.

Photoresponse

For evaluating the mobility–lifetime product $\mu\tau$, a current versus voltage measurement was obtained with the symmetrical (both contacts are Cu) laterally contacted MAPbI_3 SC under modulated light from a light-emitting diode with a wavelength of 450 nm. The sample was biased by a Keithley 236 source-measure unit, whereas the photoinduced current was restored by a lock-in amplifier (SR830, Stanford Research).

Lifetime measurements with transient photocurrent

The transient photocurrent lifetime measurements were performed with the symmetrical (both contacts are Cu) laterally contacted MAPbI_3 SC under pulsed (20–100 μs long; wavelength, 450 nm) light-emitting diode illumination. The lifetime was extracted from the exponential fit of the signal decay⁵⁵.

X-ray characterization

X-ray attenuation is calculated based on the NIST open database⁴⁷. All the X-ray irradiation experiments (except the radiation hardness test) were performed using the X-ray tube from Amptek (model Mini-X, with a Ag target). The radiation dose rate measurements are performed with a PM1621A dosimeter from Polimaster. Sensitivity measurements (Extended Data Fig. 2a) for MAPbI_3 and CdZnTe SCs are carried out with a Keithley 236 source-measure unit under X-ray irradiation at 40 kV_p (peak kilovoltage or the maximum high voltage applied across an X-ray tube). For a.c. bias measurements, the symmetrical laterally contacted MAPbI_3 SC with Cu was used. The function generator HP 8116A with an a.c. voltage amplifier (Falco Systems WMA-300) was utilized for biasing, 40 kV_p X-ray irradiation was modulated with a lead chopper wheel and the signal was restored on a lock-in amplifier (SR860, Stanford

Research). SNR, detection limit, noise and stability measurements (Supplementary Fig. 2, Extended Data Fig. 2b and Figs. 2e and 1f) were obtained with the samples connected via a low-noise current amplifier (Femto DLPCA-200) to a spectral network analyser (SR770, Stanford Research) under modulated 20 kV_p X-ray irradiation, attenuated by a 3 mm glass filter. The noise-current spectral density dependence on the dose rate (Fig. 2e) was measured at a frequency of 960 Hz with the 110- μm -thick device with an area of 0.8 mm² and resistance of 6 M Ω . The experimental DQE values (Fig. 1e) were calculated according to $\text{DQE} = \text{SNR}_{\text{detector}}^2 / \text{SNR}_{\text{ideal}}^2$, where $\text{SNR}_{\text{detector}}$ was calculated as the ratio of the average count number at certain X-ray photon flux to the corresponding r.m.s. counts, whereas $\text{SNR}_{\text{ideal}}$ was taken as $\sqrt{n_{\text{ph}}}$, where photon number n_{ph} was evaluated based on the count rate of a reference CdZnTe SC detector. The sensitivity values for DE evaluation (Fig. 2d) were estimated with modulated X-ray irradiation; the sample was connected via the low-noise current amplifier (Femto DLPCA-200) and the signal was restored by the lock-in amplifier (SR860). For the photon energies of 60 keV, we obtained DE as a ratio of the measured counting rate to the expected calculated value, taking into account the activity of the ²⁴¹Am source. The energy-resolved spectrum for the Am²⁴¹ source (activity, 0.4 MBq) was measured with a charge-sensitive preamplifier (A250CF CoolFET, Amptek) and digital-shaper amplifier based on Picoscope 2208B (for energy resolution measurements). For the maximal count rate estimation, a signal after a charge-sensitive preamplifier was treated with an analogue-shaper amplifier (Model 572, ORTEC). The shaping time was adjusted to 10 μs for the energy-resolved spectra measurements and 2 μs for the maximal counting rate experiments. After being processed with the shaper, the signal was fed to a digital multichannel analyser (MCA-8000D, Amptek). For the radiation hardness test (Supplementary Fig. 5), the 220- μm -thick device was irradiated by an X-ray tube from General Electrics. The X-ray tube current and acceleration voltage were set to 43 mA and 40 kV_p, respectively, resulting in a dose rate of 1 Gy_{air} min⁻¹. The device X-ray photocurrent stability was monitored for 14 h of continuous irradiation.

X-ray imaging

The images shown in Figs. 1d and 3e and Supplementary Fig. 4 were acquired in the single-photon-counting mode, whereas an object was 2D scanned in the lateral direction towards the single-pixel detector. The detector was connected to a charge-sensitive preamplifier (A250CF CoolFET, Amptek) and analogue-shaper amplifier (Model 572, ORTEC). The shaping time was adjusted to 10 μs . After being processed with a shaper, the signal was fed to a digital multichannel analyser (MCA-8000D, Amptek). For multicolour imaging, two amplitude thresholds were set on the MCA to obtain two energy channels. Events with amplitude below the lowest threshold were discarded (attributed to noise), whereas when an amplitude falls into the region between the first and second threshold, such event was counted as low-energy photons. Events with amplitude higher than the second threshold were counted as high-energy photons. Threshold values were adjusted to obtain the highest contrast on the reference points of the imaged object, indicating that the threshold separating the high- and low-energy channels was set near 43 keV (Fig. 3d). The image shown in Fig. 3e was obtained under a 50 kV_p X-ray irradiation filtered by a 500- μm -thick steel plate to cut the lower-energy part (the corresponding spectrum is presented in Supplementary Fig. 18a), the accumulated dose per pixel is about 10 μGy . The images shown in Fig. 1d and Supplementary Fig. 4 were obtained with 20 kV_p X-ray irradiation filtered by 3 mm glass to get a quasi-monoenergetic spectrum with a mean energy of 18 keV (Supplementary Fig. 18b). The imaging experiments with pixelated array detectors (Fig. 1h and Supplementary Fig. 7, linear; Supplementary Fig. 6, 2D pixels) were performed in the charge-integration mode, whereas the device was connected to a 64-channel application-specific integrated circuit, where each channel consists of a charge-integration amplifier connected to an

analogue–digital converter. For the linear array, an object was 2D scanned in the lateral direction towards the detector: along the X axis, the line pitch of the step was 40 μm , whereas along the Y axis, it was 80 μm . The X-ray beam was collimated with a rectangular steel aperture (vertical width, 200 μm), having a profile shown as the dashed line in Fig. 1g, inset. The vertical spatial resolution of the MAPbI₃ X-ray image (Supplementary Fig. 7, inset) is limited by the aperture size, whereas the horizontal spatial resolution is given by the intrinsic linear array properties. A commercial GOS scintillation detector, Remote RadEye HR, with a 20 μm pixel pitch was used in the imaging experiments as the reference. Images in the insets of Supplementary Fig. 7 were taken under 50 kV_p X-ray irradiation under identical geometrical conditions with an accumulated dose of 193 μGy .

MTF

The MTF curve is calculated with a linear detector array of 40 μm pitch using the slanted-edge method. The edge spread function (ESF(x)) was derived from the slanted-edge profile, obtained from the one-dimensional X-ray image of a thin steel slice under 20 kV_p X-ray irradiation. Afterwards, the MTF is calculated as

$$\text{MTF}(v) = F(\text{LSF}(x)) = F\left(\frac{d\text{ESF}(x)}{dx}\right),$$

where v is the spatial frequency and x is the position of the lines. Similar to this formula, the line spread function (LSF(x)) is the derivative of ESF(x) and MTF(v) is the Fourier transform (F) of LSF(x).

DQE

The DQE dependence on spatial frequency is calculated according to the following formula⁴⁶:

$$\text{DQE}(v) = \text{DQE}(v=0, D=5 \mu\text{Gy}_{\text{air}}) \times \frac{\text{MTF}^2(v)}{\text{NTF}(v)},$$

where $\text{DQE}(v=0, D=5 \mu\text{Gy}_{\text{air}}) = 87\%$ is obtained according to the derived model, and NTF(v) is the noise transfer function, which, for the photon-counting detector, is assumed⁴⁶ to be independent of spatial frequency and equal to 1.

Data availability

All relevant data supporting the findings of this study are available within the article and its Supplementary Information. Source data are provided with this paper.

References

- Sze, S. M. *Semiconductor Devices: Physics and Technology* 60–63 (Wiley, 2002).

Acknowledgements

The work at ETH Zürich was financially supported by the Swiss Innovation Agency (Innosuisse) under grant agreement 46894.1 IP-ENG and by ETH Zürich through the ETH+Project SynMatLab: Laboratory for Multiscale Materials Synthesis. We acknowledge funding support from the King Abdullah University of Science and Technology (KAUST) and the use of KAUST Core Lab and KAUST Solar Center facilities. We also acknowledge F. Geser, A. Stabilini and M. Kasprzak from the Verification and Calibration Laboratory of the Paul Scherrer Institut (Switzerland) for their assistance in the radiation hardness measurements.

Author contributions

K.S. measured the X-ray and noise performance, formulated the detector figure-of-merit requirements, performed the X-ray imaging experiments and analysed the results, with contribution from G.J.M. and S.Y. G.J.M., K.S. and S.Y. measured the charge transport

characteristics. B.T. developed the MAPbI₃ SC growth, fabricated the XPV devices, characterized them under one-sun illumination and measured the external quantum efficiency. M.N.L. performed the scanning electron microscopy measurements. B.T. and R.N. fabricated the devices for ToF measurement. E.W. and V.B. developed and fabricated the patterned conductive substrate with the corresponding readout printed circuit boards. K.S. and A.S. performed the spatial resolution characterization and imaging experiments with multiple-pixel samples. K.S., S.Y. and M.V.K. wrote the paper with the contribution of all the co-authors. M.V.K., S.Y., I.S., O.F.M. and O.M.B. supervised the work. K.S. and B.T. contributed equally to this work. All the authors discussed the results and commented on the paper.

Funding

Open access funding provided by Swiss Federal Institute of Technology Zurich.

Competing interests

The authors declare no competing interests.

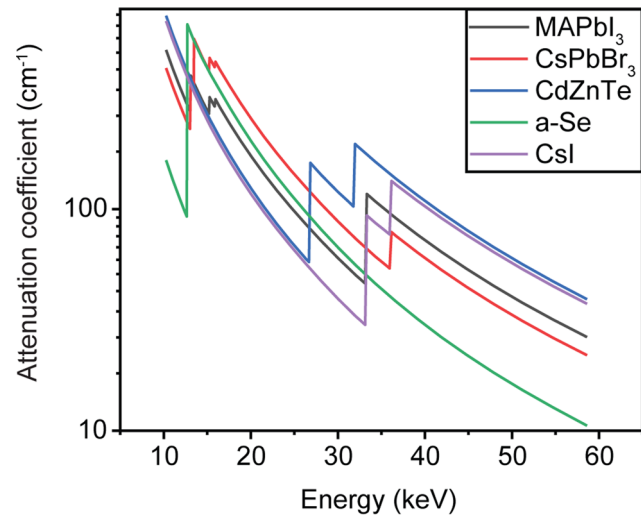
Additional information

Extended data is available for this paper at <https://doi.org/10.1038/s41566-023-01207-y>.

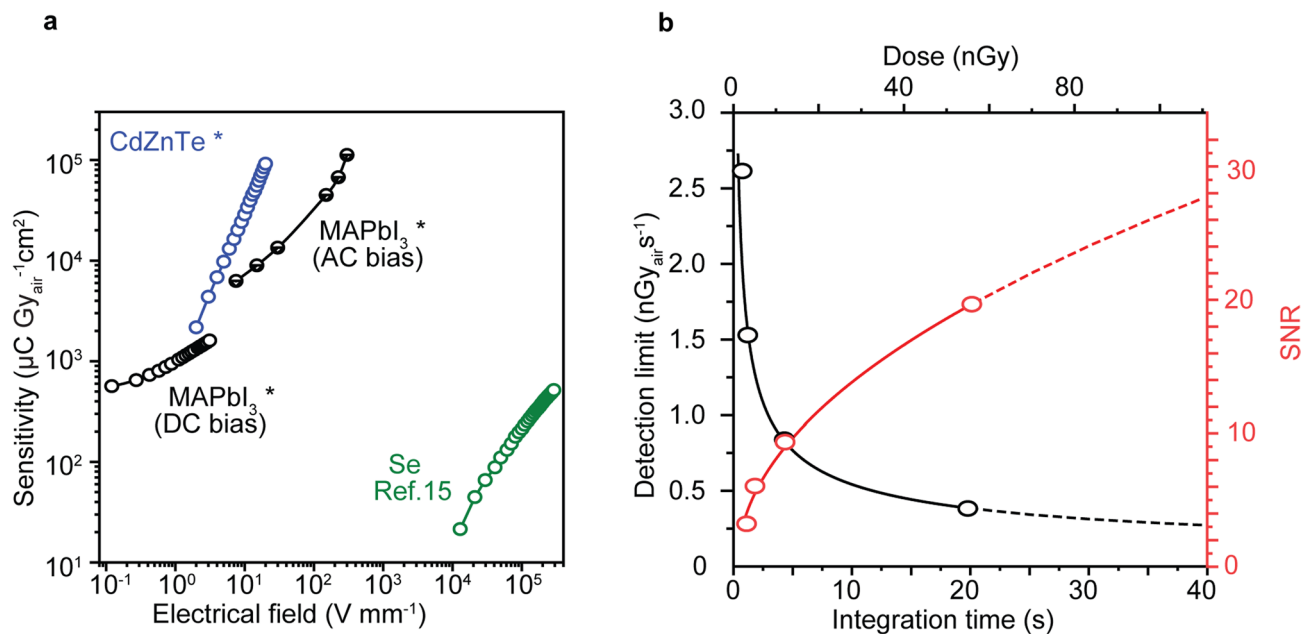
Supplementary information The online version contains supplementary material available at <https://doi.org/10.1038/s41566-023-01207-y>.

Correspondence and requests for materials should be addressed to Sergii Yakunin, Osman M. Bakr or Maksym V. Kovalenko.

Reprints and permissions information is available at www.nature.com/reprints.

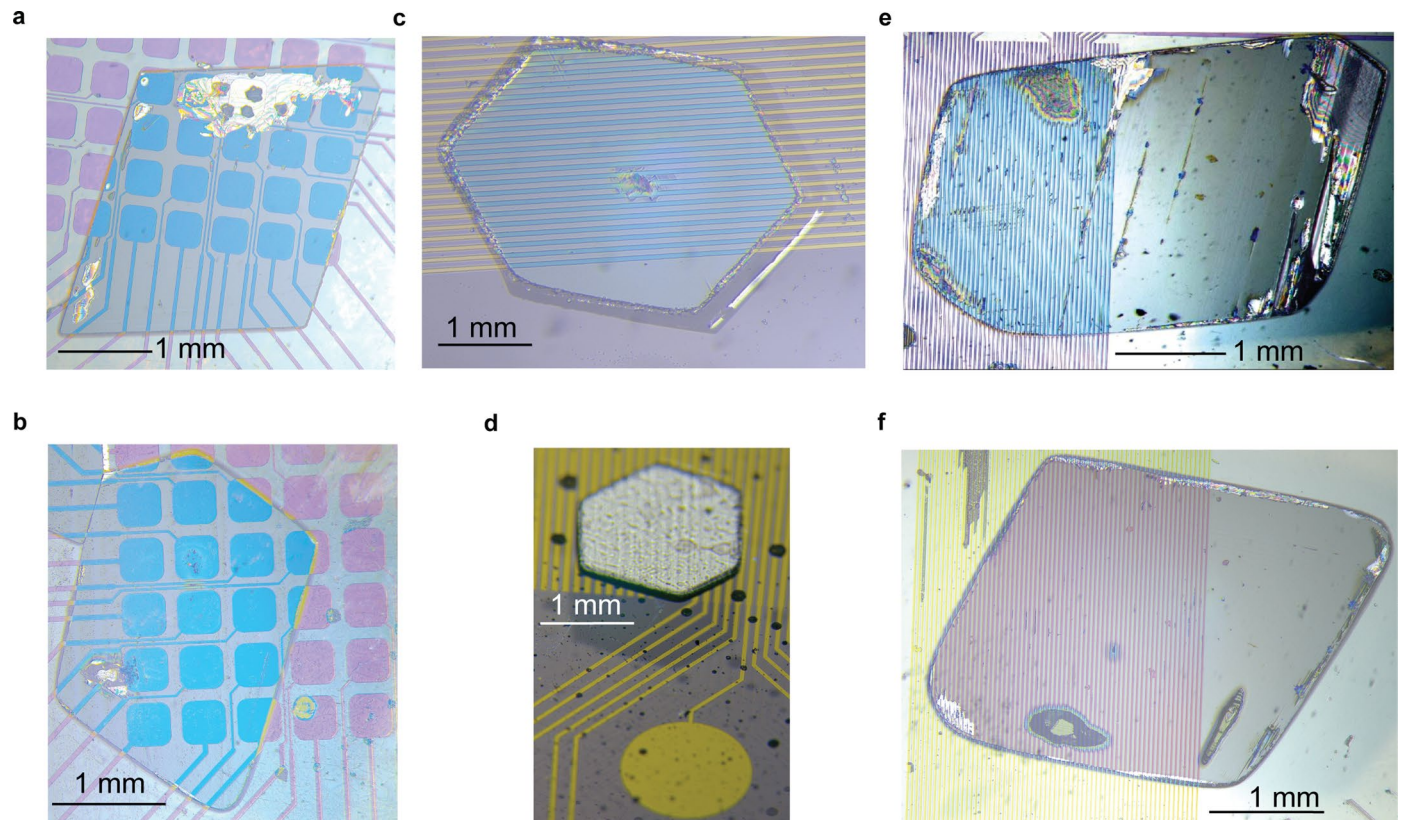


Extended Data Fig. 1 | X-ray attenuation coefficient dependence on X-ray energy. They are calculated for materials commonly used in X-ray detectors using tabulated atomic coefficients⁴⁷.



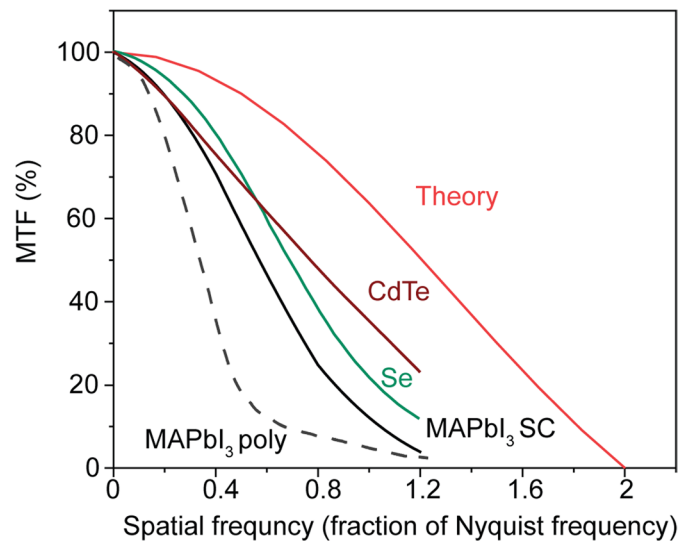
Extended Data Fig. 2 | X-ray detection figures-of-merits, commonly used for perovskites. a, X-ray sensitivity dependence on the electric field for different materials. Superior sensitivity at AC bias is achieved by suppression of ion

accumulation effects. **b,** Decrease of detection limit and increase of SNR at longer integration times come at the cost of a high dose, for a MAPbI₃ SC XPV detector under X-ray irradiation.

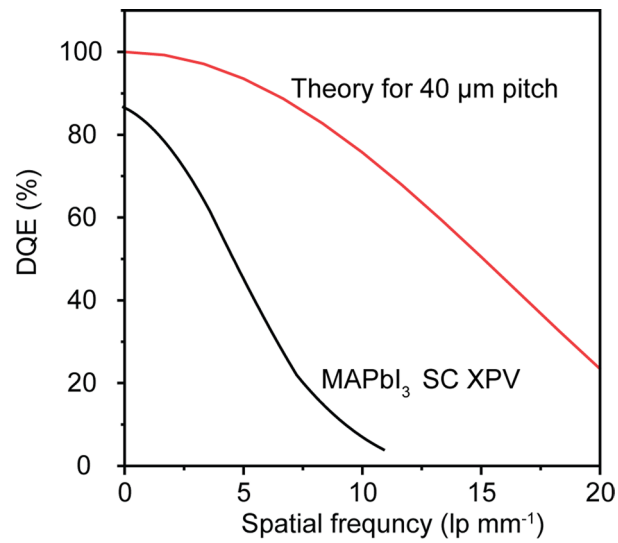


Extended Data Fig. 3 | Photographs of MAPbI₃ SCs grown directly on patterned, conductive ITO substrate. a-b, Crystals grown on the pixelated pattern viewed through ITO (bottom) layer. The pixel pitch is 500 μm. **c-d**,

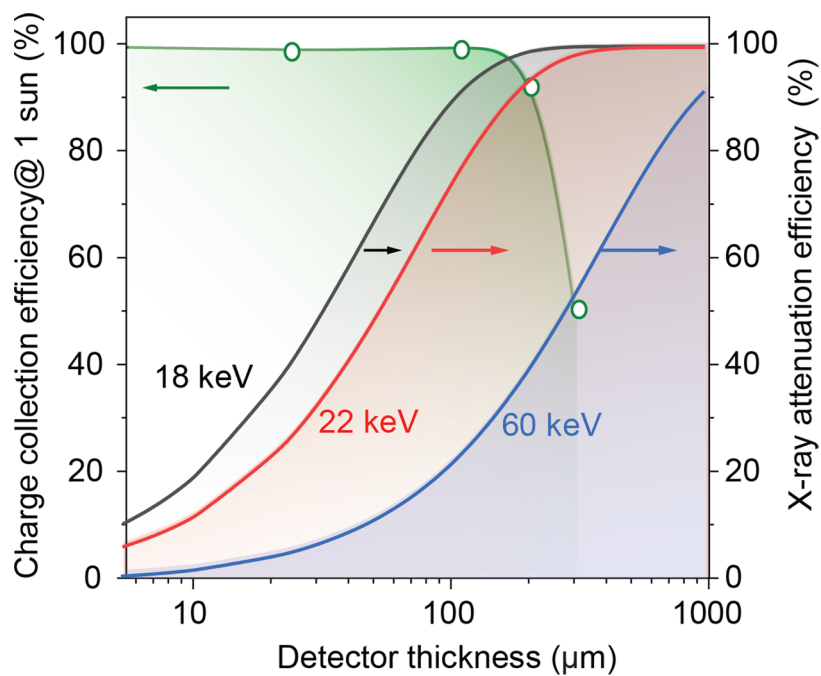
Bottom (c) and top (d) views of crystals grown on the linear array. The line pitch is 120 μm. **e-f**, Bottom pictures of large crystals grown on the linear array. The line pitch is 40 μm. Scale bar length is 1 mm in every image.



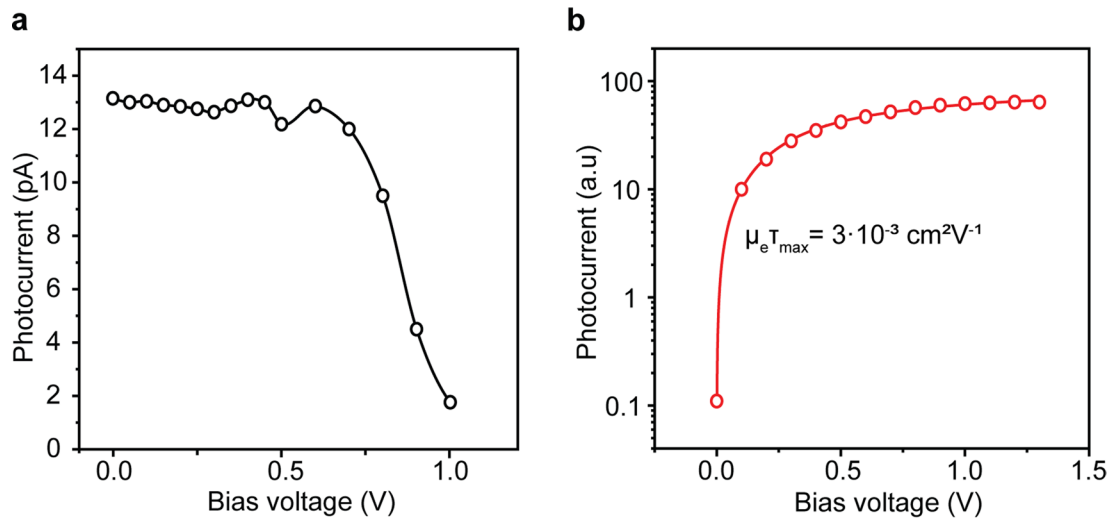
Extended Data Fig. 4 | Modulation transfer function dependencies on normalized spatial frequency. Values are estimated for a theoretical limit (red line) and commercial detectors - 75 μm pitch CdTe SC³⁴ (brown line), 70 μm pitch a-Se¹⁵ (green line); perovskite MAPbI₃ SC with 40 μm pitch in XPV mode (solid black line), polycrystalline MAPbI₃ layer 70 μm pitch¹³ (black dashed line).



Extended Data Fig. 5 | DQE dependence on spatial frequency. Values are estimated for 40 μm pitch and 110 μm thick MAPbI₃ SC XPV device (black) and theoretical limit for 40 μm pitch detector (red line) for 18 keV X-ray energy.

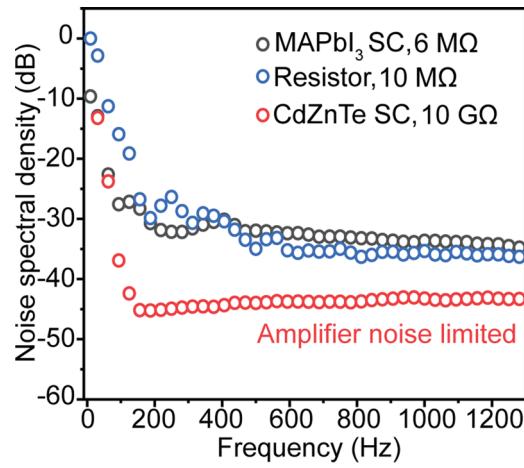


Extended Data Fig. 6 | Charge-collection efficiency and X-ray attenuation efficiency thickness dependencies for MAPbI₃ SCXPV devices. Charge-collection efficiency is evaluated for illumination with optical photons at zero-bias and X-ray attenuation efficiency is shown for various X-ray energies, given in different colors.



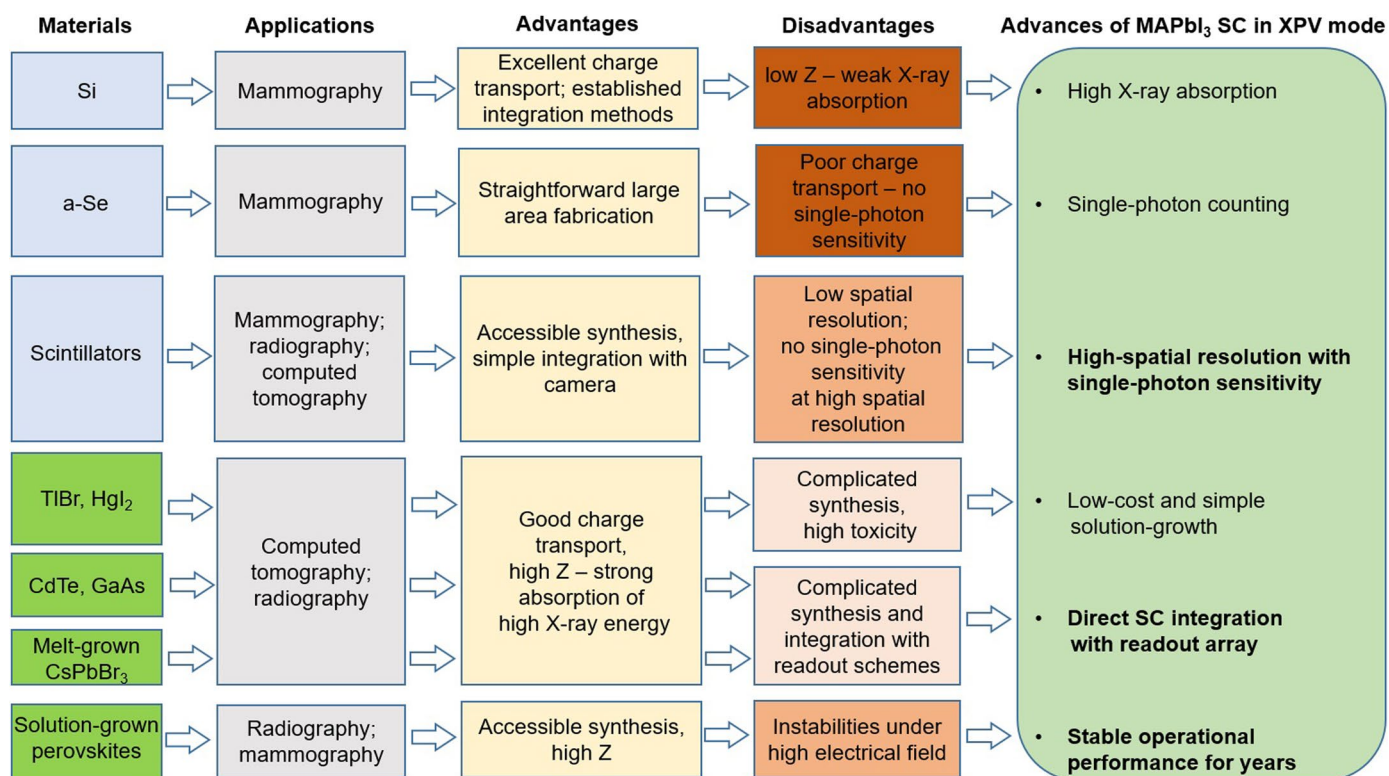
Extended Data Fig. 7 | Determination of the open-circuit voltage and $\mu\tau$ -product. **a**, Photo-induced current *vs.* bias voltage dependence for MAPbI₃ XPV device (thickness is 330 μ m) under 50 kVp X-rays, with open-circuit voltage

$V_{oc} \approx 1.05$ V. **b**, Photocurrent-bias voltage dependence for symmetrically contacted Cu/MAPbI₃/Cu device. Photoresponse is fitted with the Hecht equation to determine $\mu\tau$.



Extended Data Fig. 8 | Thermal noise spectra. Measurements were taken with the spectral analyzer SR770, and the low-noise current amplifier (Femto DLPCA-200) at $\times 10^{11}$ amplification coefficient for different test samples with no external bias voltage applied. It is seen that the noise for MAPbI₃ SC (of 6 MΩ

internal resistance) is just slightly higher than the thermal noise for the 10 MΩ resistors. For CdZnTe SC (of 10 GΩ internal resistance), the noise is limited by the amplifier.

Extended Data Table 1 | Application, advantages, problems of current X-ray detector materials and advances of MAPbI₃ SC XPV device

The leftmost panel lists commercial (blue) and in-development (green) X-ray detector materials. The second (from left) panel lists their applications in medical diagnostics. The middle panel lists material-related advantages as X-ray detection. The fourth panel lists material-specific challenges, whereas the color depth signifies their criticality. The rightmost panel summarizes specific advances of MAPbI₃ SC XPV, with bold text emphasizing this work. The combination of these features is unique to MAPbI₃, that is not offered by materials on the left.